Density Functional Theory Modeling of Photo-electrochemical Reactions on Semiconductors: H$_2$ Evolution on 3C-SiC

Published as part of The Journal of Physical Chemistry virtual special issue "Emily A. Carter Festschrift".

Manav Bhati,[†] Yu Chen,[†] and Thomas P. Senftle*

Cite This: *J. Phys. Chem. C* 2020, 124, 26625−26639

Read Online

ACCESS | Metrics & More | Article Recommendations | Supporting Information

ABSTRACT: We develop a protocol for modeling photo-electrochemical reactions on semiconductor surfaces using density functional theory (DFT). We use an implicit solvation model of the electrolyte to implement an electronic grand canonical formalism for treating the variable charge state of the semiconductor surface under illumination and an applied bias. This protocol is applied to investigate the photodriven mechanism of the hydrogen evolution reaction (HER) over a cubic silicon carbide (3C-SiC) surface, which demonstrates that a Heyrovsky H$_2$ generation step is rate-determining on the SiC (110) surface. The reaction free energy barrier of this step is heavily influenced by the surface charge density that is controlled by illumination and applied bias. The computed photon wavelengths required to overcome the Heyrovsky step barrier fall in the visible spectrum, thereby establishing the feasibility of HER reactions on the SiC (110) surface. Beyond offering insight into the HER mechanism on SiC, this work provides a general framework for modeling photo-electrochemical reactions occurring at an interface between a semiconductor surface and a liquid electrolyte.
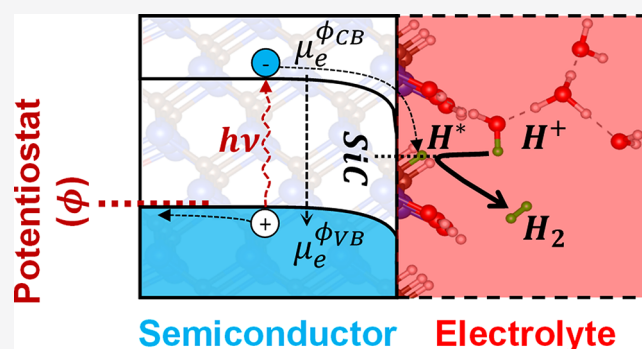
1. INTRODUCTION

Modeling photo-electrochemical (PEC) reactions at solid electrode/liquid electrolyte interfaces is challenging.[1−3] A key hurdle in modeling electrochemical reactions occurring at a constant applied potential is devising a protocol for adjusting the number of electrons in the simulated electrode to maintain a constant potential throughout the reaction. With such a protocol, the electrode potential can be controlled by varying the charge density on the electrode surface until the proper work function matching the target potential is obtained. It is not trivial to vary the charge density (i.e., the number of electrons) in a periodic simulation cell, since one must include an appropriate counter charge scheme to maintain cell neutrality. These problems can be tackled with implicit solvation models, where the concentration and distribution of counterions in the electrolyte can effectively screen the charged state of the electrode,[4,5] thus satisfying the condition of a neutral periodic system. Implicit solvation models are also advantageous when explicit treatment[6−9] of a large number of electronic and ionic degrees of freedom associated with electrode/electrolyte interfaces becomes computationally intractable.[10] For example, the VASPsol[4,5] model, implemented in the Vienna *ab initio* simulation package (VASP),[11,12] provides a description of electrode/electrolyte interfaces by combining the solutions of density functional theory (DFT) describing electron density in the electrode with

those of linearized Poisson−Boltzmann equations describing the electrolyte. Using this scheme, one can control the charge state of the electrode to determine reaction energetics as a function of electrode potential. This approach has been implemented successfully to investigate electrochemical reactions on several metal/electrolyte systems under a constant applied potential.[13−18] However, a similar implementation on semiconductor/electrolyte systems under photoelectrocatalytic conditions has not been reported yet to the best of our knowledge.

Unlike metallic systems, the accessible range of electron chemical potentials in a semiconductor is not continuous because of the bandgap. Simulating processes that inject electrons into the system will induce a substantial shift in the system's work function, as the added electrons must traverse the bandgap to occupy the conduction band. Thus, modeling electrochemical reactions in a constant-electron formalism that requires electrons to be added to or removed from the
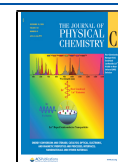
electrode surface during a reaction will cause an unphysical shift in the electrode's work function. This issue can be remedied with models to determine the cell extrapolation limit where the change in surface charge density vanishes.[19,20] Here, we apply a variable-electron framework for modeling PEC reactions on semiconductor electrodes by unambiguously defining the electron chemical potential at each elementary reaction step based on the applied potential and the energy of photoexcited electrons in the conduction band under illumination. The photoexcitation step is treated as an explicit elementary step, thus accounting for the energy provided to the system via illumination. We take the hydrogen evolution reaction (HER) on cubic silicon carbide (3C-SiC) as our model reaction for developing this protocol, as the HER mechanism on 3C-SiC surfaces is not well understood.

Efficient production of hydrogen (H_2) from water splitting using renewable solar energy is a long-term sustainable remedy for simultaneously alleviating the global energy and environmental crisis.[21] PEC water splitting using semiconductor electrodes is a promising technology for renewable hydrogen production.[22] 3C-SiC is an attractive candidate photoelectrocatalyst for this reaction because its bandgap is suited for visible light absorption (2.36 eV) and its band edges straddle the redox potentials of the HER and the oxygen evolution reaction (OER).[23] Furthermore, SiC is chemically stable, corrosion-resistant, and environmentally friendly, making it even more practical for PEC water splitting applications. In earlier attempts to improve HER activity over 3C-SiC, He et al.[24] showed that reducing the size of the SiC nanocrystals enhanced its autocatalytic properties and improved HER activity. Higher activity was attributed to the reduced activation barrier for water dissociation on the surface, and also to a higher specific surface area. They showed that HER activity would be negligible in basic conditions due to low coverage of surface H, suggesting a critical role of surface adsorbed species, particularly H, in the reaction mechanism. In addition, using SiC as a photocathode significantly improved its HER performance compared to operation in the dark, emphasizing the beneficial role of photoexcitation in the HER mechanism. Yasuda et al.[23] doped several polytypes (3C-, 4H-, 6H-) of SiC with p-type impurities and showed that photodriven HER could be achieved with solar irradiation on all SiC polytypes even in the absence of an applied bias. These early successes motivated other studies in several directions,[25] such as doping SiC with p/n-type impurities,[26,27] using cocatalysts,[26] modifying the surface via acid oxidation,[28] using heterostructure composites,[29−32] and engineering various SiC nanostructures.[33−36]

These studies revealed avenues for enhanced HER performance and established SiC as a promising photoelectrocatalyst, but details regarding the mechanism of HER on SiC still are largely unknown. Shen et al.[37] investigated the HER mechanism on a cluster model of 3C-SiC in an implicit solvation environment. However, cluster models provide a less reliable description of the electronic structure of the extended system, which necessitates slab models with periodic boundaries.[38] An accurate description of the electronic structure is especially important when modeling PEC reactions, as the reaction mechanism and energetics are dependent on the electron chemical potential (i.e., on the electrode potential). Nevertheless, that work demonstrated that, contrary to the typical Volmer−Heyrovsky HER mechanism on metals, the Heyrovsky reaction precedes the

Volmer reaction on a prehydrogenated SiC surface, which has motivated the HER mechanism proposed in our work here, initiating from a SiC surface covered with H and OH adsorbates from dissociated water. In their investigation of the Heyrovsky−Volmer HER mechanism, explicit electrons were added to the cluster model to determine the feasibility of reaction steps under varying charge states, but the reaction energies and activation barriers were not reported. Du et al.[39] used DFT calculations to investigate an HER mechanism on various facets of 3C-SiC, where they used a slab model featuring the Si-terminated (111) facet. They proposed that the HER mechanism proceeds through the dissociative adsorption of water, where hydrogen is generated by dissociating the O−H bond of adsorbed OH groups to generate O on the surface. That work only considered water adsorption and dissociation in the vacuum on the clean surface, and thus the proposed mechanism reflects a thermal catalytic mechanism and not a photo-electrochemical mechanism on a solvated surface.

Although these previous studies have provided useful insight, further work is needed to elucidate the HER mechanism on 3C-SiC surface structures that are representative of the photo-electrochemical operating conditions. In this work, we first investigate the suitability of the VASPsol implicit solvation model for describing the solvated 3C-SiC (110) surface. Upon validation, we apply this solvation model to investigate the HER mechanism on the 3C-SiC (110) surface under a constant applied potential and illumination by implementing an electronic grand canonical formalism. The methods developed here are generally applicable for modeling PEC reactions at semiconductor/electrolyte interfaces.

2. COMPUTATIONAL METHODS

2.1. DFT Settings, Solvation Model, and 3C-SiC Geometries. We performed DFT calculations with VASP 5.4.4[11,12] in conjunction with VASPsol.[4,5] The Perdew−Burke−Ernzerhof (PBE)[40] generalized gradient approximation of the exchange-correlation functional was employed for all the calculations. Some reaction energies, density of states (DOS), and charge localizations also were computed using the strongly constrained and appropriately normed (SCAN)[41] and Heyd−Scuseria−Ernzerhof (HSE06)[42] functionals as a benchmark for understanding the accuracy of the PBE functional applied to the SiC system. The default projector augmented wave (PAW)[43] potentials were used for all nuclei and frozen core electrons, and the valence electrons of C-$2s^2 2p^2$, Si-$3s^2 3p^2$, O-$2s^2 2p^4$, and H-$1s^1$ were treated self-consistently. All calculations were spin-polarized. We performed energy convergence tests to determine a kinetic energy cutoff of 500 eV for truncating plane-wave basis sets and a Monkhorst−Pack (MP)[44] k-point mesh of 3 × 3 × 1 to sample the Brillouin zone for a (3 × 2) periodic SiC (110) slab. Gaussian smearing was employed with a smearing width of 0.05 eV to integrate the Brillouin zone. We did not include van der Waals corrections to avoid uncertainties in the implicit solvation model, which can easily arise due to the nontransferability of the implicit solvation parameters when mixed with a separate van der Waals model.[2] Geometry optimizations were converged to forces within 50 meV Å^{-1}. The electronic energy was converged to within 10^{-5} eV for each electronic self-consistent-field cycle. The climbing image nudged elastic band (CI-NEB)[45,46] method was used to locate transition states (TS), which was combined with the dimer method[47] to refine

the search for saddle points. Each TS structure was confirmed to have one imaginary frequency corresponding to the reaction coordinate at the saddle point. Dipole corrections were not applied perpendicular to the surface because the continuum solvation model screens any net dipole. This was confirmed by plots of the planar average of the local electrostatic potential in the simulation cell along the z-direction (shown in Figures S1 and S2 of the Supporting Information). These plots show that, with implicit solvation, the potential is constant and continuous in the electrolyte region, irrespective of the symmetry of the slab. Also, Gauthier et al.[2] showed that the choice to use a symmetric or asymmetric cell would have only a small effect on the energetics.

In VASPsol, the ion distribution is determined by four parameters: the relative permittivity of the bulk solvent (ε_b), the electron density cutoff ($\tilde{\rho}_{el,cut}$), the dimensionless smoothness parameter (σ) that determines the width of the diffuse cavity, and the effective surface tension (τ).[4,5] Default parameters for VASPsol are 78.4, 2.5×10^{-3} Å^{-3}, 0.6, and 5.25×10^{-4} eV Å^{-2}, respectively.[4,5] The electrolyte in our system consists of an aqueous solution of monovalent anions and cations at 1 M concentration, which is determined by setting $\varepsilon_b = 78.4$ and a Debye screening length of $\lambda_D = 3.04$ Å.[5] Gauthier et al.[2] showed that the local electrostatic potential can be numerically unstable in the interface region and oscillates in the electrolyte region if the default effective surface tension parameter is used and that these instabilities are removed if $\tau = 0$. We observed similar behavior and therefore we set $\tau = 0$ throughout this work. We employed default values for the rest of the parameters. The electrolyte spacing between the periodic slab images perpendicular to the surface was determined through convergence tests for the surface formation energy, bandgap center, and ionic countercharge concentration. Generally, it is sufficient to have an electrolyte region greater than $\sim 10\lambda_D$, which characterizes the electrochemical double layer dimension.[17] Based on our convergence test we determined that an implicit electrolyte region of 35 Å was necessary, in agreement with the $\sim 10\lambda_D$ heuristic. We performed convergence tests for the number of SiC layers and determined that a six-layered slab is well-converged, yielding surface formation energies within 1 meV Å^{-2} and bandgap center positions within 0.1 eV.

Earlier studies of HER on SiC employed SiC (111) and (100) surfaces that either were clean[39] or covered with hydrogen.[37] However, a recent study by Peng et al.[48] derived the thermodynamic phase diagram for various SiC facets, which revealed that the stoichiometric (110) surface is the most stable under the range of operating conditions relevant to our study. They found that water readily dissociates on the clean SiC (110) surface (Figure 1a), such that surface hydroxyl and hydrogen adsorb on Si and C surface sites, respectively, forming a hydrogen-bonded network on the surface.[48] Accordingly, we employed a SiC (110) surface slab model with a dissociated water layer on both sides of the SiC (110) slab (Figure 1b). This arrangement also saturates all dangling bonds on the surface, so there are no defect states present in the semiconductor bandgap. A combined explicit–implicit approach is expected to provide a better description of solvation and stabilization of reaction intermediates through hydrogen bonding.[2,14] For this reason, we treat the solvated proton using an Eigen cation (i.e., H_3O^+ $(H_2O)_3$), where the central hydronium is stabilized with hydrogen bonds from three surrounding water molecules (Figure 1c). The Eigen
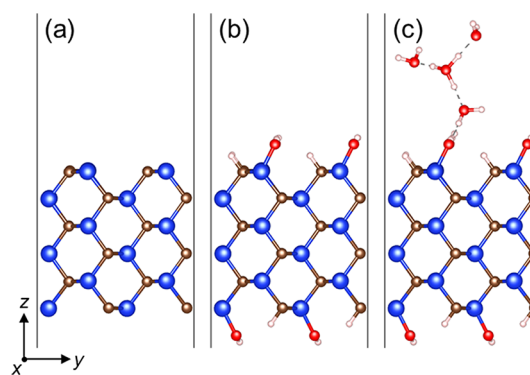
Figure 1. Geometries of periodic slab models for (3×2) 3C-SiC (110): (a) clean surface, (b) surface covered with a dissociated water layer on both sides, and (c) surface covered with a dissociated water layer on both sides in the presence of an Eigen cation (blue: Si, brown: C, red: O, white: H, dashed lines: hydrogen bonds).

cation is oriented such that one of its water molecules can act as a mediator to shuttle a proton from the hydronium to the surface during HER.

2.2. Bandgap Calculations. We applied the methodology from the work of Toroker et al.[49] to compute the band edge positions of solvated 3C-SiC (110). First, the bandgap center position referenced to vacuum (E_{BGC}) was determined using the PBE functional on the SiC (110) slab model. Second, the quasi-particle bandgap (E_g) was determined with a nonself-consistent many-body Green function (G_0W_0)[50,51] calculation on a bulk SiC unit cell containing one Si atom and one C atom. The G_0W_0 calculation employed an $8 \times 8 \times 8$ Γ-point-centered k-point mesh, 500 eV kinetic energy cutoff, 96 bands, and 96 frequency grid points. Using the E_{BGC} and E_g, the position of the valence band maximum (E_{VBM}) and conduction band minimum (E_{CBM}) were calculated using eqs 1 and 2:[49]

$$E_{VBM} = E_{BGC} - \frac{1}{2}E_g \tag{1}$$

$$E_{CBM} = E_{BGC} + \frac{1}{2}E_g \tag{2}$$

Because our calculation for band edge positions was performed with a neutral surface, the band edge positions correspond to positions at the pH of zero charge (pH$_{zc}$). We assume that pH$_{zc}$ = 7 for the SiC (110) surface in this work because there is an even coverage of protons and hydroxides predicted under neutral conditions,[38,48] and in Section 3.1 we test the sensitivity of our results with respect to this assumption. We utilized the Nernst relation, as formulated in eqs 3 and 4, to compensate for the shifts in band edge positions caused by the difference between the electrolyte pH and the pH$_{zc}$. The electrolyte is considered at pH = 0 to refer the entire system to the standard hydrogen electrode (SHE) scale and to resemble the experimental system under acidic conditions.[24]

$$E_{VBM}^{pH} = E_{VBM}^{pH_{zc}} + 0.059(pH - pH_{zc}) \tag{3}$$

$$E_{CBM}^{pH} = E_{CBM}^{pH_{zc}} + 0.059(pH - pH_{zc}) \tag{4}$$

The energies in eqs 1–4 are formulated on the SHE scale by referencing E_{BGC} to the chemical potential of an electron at SHE relative to vacuum. The band edge positions relative to 0 V_{SHE} are determined as follows:

$$\phi_{BE} = (\mu_{e,vac}^0 - E_{BE})/e \tag{5}$$

where ϕ_{BE} is the band edge position (either CBM or VBM) relative to 0 V_{SHE}, e is the positive elementary charge, E_{BE} is the energy of the band edge determined from eqs 3 and 4, and $\mu_{e,vac}^0$ is the chemical potential of an electron at 0 V_{SHE} referenced to the vacuum. We use the empirical value of −4.44 eV for $\mu_{e,vac}^0$.[52] We also tested the effects of the VASPsol implicit solvation model on the band edge positions, where $\mu_{e,vac}^0$ in eq 5 is replaced with the appropriate bulk electrolyte reference[5] if VASPsol implicit solvation is used ($\mu_e^0 = -4.6$ eV). The offset of ∼0.16 eV is within the typical range for continuum solvation models.[53]
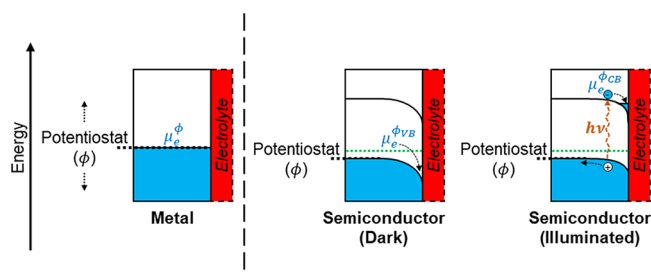
2.3. Chemical Potential of Electrons under an Applied Potential.

The chemical potential of electrons under an applied bias is determined by the fixed electrode potential. In metal electrodes, the continuous band allows the potentiostat to directly control the chemical potential of electrons by the relationship:

$$\mu_e^\phi = \mu_e^0 - e\phi \tag{6}$$

where μ_e^ϕ is the chemical potential of the electron in the electrode at potential ϕ and μ_e^0 is the chemical potential of the electron at 0 V_{SHE} referenced to the bulk electrolyte. ϕ is expressed on the SHE scale by using the empirical reference of $\mu_e^0 = -4.6$ eV reported for the VASPsol description of the bulk electrolyte.[5] The chemical potential of the electron in the electrode referenced to the bulk electrolyte (μ_e^ϕ) is related to the Fermi level (ϕ_F) corresponding to the highest occupied state and the bulk electrolyte potential ($\phi_{electrolyte}$) as follows:

$$\mu_e^\phi = -e(\phi_F - \phi_{electrolyte}) \tag{7}$$

For semiconductor electrodes, a similar relationship between the chemical potential of electrons and applied electrode potential exists, but it is broken inside the potential range corresponding to the bandgap of the material (Figure 2). A potential applied in the range of the bandgap is not sufficient to alter the occupancy of states in the material, and the chemical potential of the electrons remains at the valence band edge. The electrons acquire sufficient energy to occupy states

Figure 2. Schematic to illustrate the effect of the potential (ϕ) applied by a potentiostat on the chemical potential of electrons (μ_e) in metal and p-type semiconductor electrode surfaces under dark and illuminated conditions. $h\nu$ is the energy of the photon required to excite an electron across the bandgap. The blue color represents filled states. The black and green dashed lines in the band diagrams represent the set potential of the potentiostat and the Fermi level of the electrode surface, respectively. In this work, we consider that the potentiostat is set such that the chemical potential of the electron is equal to the potential of the valence band edge (ϕ_{VB}) of the semiconductor surface (by eq 8 in the text).

in the conduction band only if the applied potential is large enough to overcome the bandgap or when they interact with photons that are sufficiently high in energy. The electron chemical potential therefore is determined by the applied potential, the nature of the photoexcitation, and the position of the band edges, which are in turn influenced by band bending[54] at the semiconductor/electrolyte interface as shown in Figure 2. As such, we define the relationship between the applied potential and the electron chemical potential in a piecewise fashion:

$$\mu_e^\phi = \mu_e^0 - e\phi_{VB}, \quad \text{if } \phi_{CB} < \phi < \phi_{VB}$$
$$\mu_e^\phi = \mu_e^0 - e\phi, \quad \text{otherwise} \tag{8}$$

where ϕ_{CB} and ϕ_{VB} are the potentials of the conduction and valence bands at the semiconductor/electrolyte interface. In this work, we assume that the potentiostat is held at a constant potential that is equal to the potential of the valence band edge (ϕ_{VB}). In this way, any vacancy in the valence band is filled by an inflow of electrons from the potentiostat at $\mu_e^{\phi_{VB}}$. During photoexcitation, an electron is excited to the conduction band, and we assume the hole in the valence band immediately is filled with an incoming electron from the potentiostat, increasing the negative charge on the electrode.[54] Finally, we use the computational hydrogen electrode (CHE) model[55] to reference the chemical potentials of the aqueous proton at pH = 0 ($\mu_{H^+}^0$) to the chemical potential of gas phase H_2 at 1 bar and 298 K ($\mu_{H_2}^0$) and the chemical potential of an electron at 0 V_{SHE} referenced to the vacuum ($\mu_{e,vac}^0$). This yields

$$\mu_{H^+}^0 = \frac{1}{2}\mu_{H_2}^0 - \mu_{e,vac}^0 \tag{9}$$

2.4. Determination of Potential-Dependent Surface Charge Density.

The constant-potential nature of the experimental conditions is formally treated in simulations with an electronic grand canonical ensemble, in which the system is held at constant electron chemical potential and is allowed a variable number of electrons.[10,53] Such an ensemble can be modeled using grand canonical self-consistent field (SCF) algorithms,[56] which can maintain the electron chemical potential by varying the number of electrons directly within the SCF cycle. Alternatively, we use a canonical SCF approach with VASPsol[4,5] in which we achieve SCF convergence for a set number of electrons in the system, determine the resulting electron chemical potential, and then iteratively adjust the number of electrons in the system to match the desired potential. On the electrolyte side, the implicit solvation model solves the linearized Poisson−Boltzmann equations to obtain the counterion charge distribution that screens the extra charge in electrode, making the overall system neutral. We sample the chemical potentials of reaction intermediates over a range of surface charge density to assess the reaction mechanism energetics under varying surface charge states dictated by the applied potential and the degree of photoexcitation.

We note that other parameters and phenomena (e.g., doping concentration, band bending, carrier mobility, recombination rates, etc.) influence the charge state of the semiconductor surface and thereby the energetics of the photo-electro-chemical reaction. However, these phenomena are specific to the experimental system, and we do not make any *a priori* assumptions about the specific surface charge state because it will be dependent on specific properties of the semiconductor

in any particular experimental setup. Our model simply derives reaction energetics as a function of the surface charge.

2.5. Calculation of Reaction Energies and Barriers. The total DFT energies from VASP of all charged systems were corrected by adding a $-Q\phi_{electrolyte}$ term, where $-Q$ is the net counterion charge in the electrolyte and $\phi_{electrolyte}$ is the electrostatic potential in the bulk electrolyte.[57] The reaction energies and barriers between species that have a different number of electrons (Δn_e) were computed by including the energy change associated with the electron chemical potential: $\Delta n_e \mu_e^\phi$. This is equivalent to the grand potential energy ($\Delta\Omega$) formalism used frequently in the literature.[13,14] The zero-point vibrational energy and entropic contributions were added to the 0 K reaction energies and barriers to obtain reaction free energies and barriers at 298 K. For these contributions, we considered the vibrational modes of only the reacting hydrogen atoms, as we assume that the contributions from all the other surface and water atoms cancel.

3. RESULTS AND DISCUSSIONS

3.1. Band Edge Positions of 3C-SiC. We first determined the bandgap and band edge positions of the 3C-SiC (110) surface to validate our choice of the surface slab model and other computational settings. In Figure 3a, the band edge alignment of SiC (110) covered with the dissociated water layer is shown along with the positions of HER (0 V_{SHE}) and OER (1.23 V_{SHE}) potentials. We also calculated the band edge
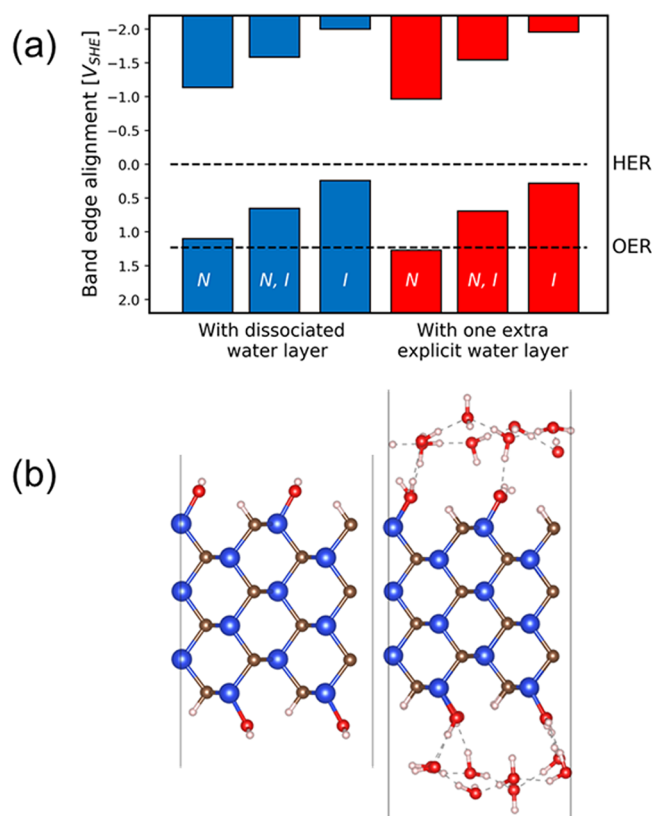

Figure 3. (a) Band edge alignments and (b) unit cell geometries of SiC (110) covered with a dissociated water layer in the absence (blue) and presence (red) of an extra explicit water layer. The labels inside the bars denote the corrections applied while calculating the band edges: N - Nernstian, I - implicit solvation (blue: Si, brown: C, red: O, white: H, dashed lines: hydrogen bonds).

alignment for an explicitly solvated slab, where a layer of explicit water is added to each side of the surface beyond the dissociated water layer as shown in Figure 3b. This model depicts a more realistic system, where the dissociated water layer is stabilized with hydrogen bonds from the explicit water molecules and is similar to the water cluster model that we use later to investigate the HER mechanism. Here, we add explicit water layers to both sides of the slab to avoid dipoles in the periodic system, as the continuum solvation, which screens any net dipole, is not present in all cases. We use an asymmetric slab model with an Eigen cation adsorbed to one side of the slab when studying the HER reaction, as the net dipole always is screened by the implicit solvation model.

The band edge alignments were first computed without implicit solvation using eqs 1−5, where the bandgap center was determined using PBE and the bandgap magnitude was determined using a G_0W_0 calculation.[49] For both surface models, we also computed the band edges with and without the Nernstian correction (eqs 3 and 4) and implicit solvation, as shown in Figure 3a with labels N and I. The band edge positions of the explicitly solvated SiC (110) surface model with the Nernstian correction straddle both redox potentials of water, supporting the water-splitting capabilities of SiC. Both the Nernstian correction (computed assuming pH_{zc} = 7) and the implicit solvation model influence the band edge alignments significantly, which has implications for the feasibility of OER over this surface because the suitability of the calculated VBM alignment for OER depends on the applied model. However, the key result for the current study is that the SiC (110) surface is always suitable for HER since the CBM is high enough irrespective of the surface model, Nernstian correction, or use of implicit solvation. The relative position of the CB and the HER potential confirms the thermodynamic feasibility of HER over the 3C-SiC surface but does not provide any information on the kinetic feasibility of the reaction, which will be determined later with the estimation of kinetic barriers. Moreover, the calculated bandgap of 2.23 eV is close to the experimental bandgap of 2.36 eV for 3C-SiC,[25] thus validating our SiC surface structure models and other computational settings.

3.2. Investigating VASPsol Performance for 3C-SiC. We examined the performance of VASPsol implicit solvation applied to the SiC (110) surface by determining the placement of ionic countercharges and the surface charge density as a function of potential. Challenges in applying implicit solvation models to study electrochemical systems were thoroughly investigated by Gauthier et al.,[2] who assessed the performance of VASPsol when modeling electrochemical events on metal surfaces. Using default VASPsol parameters, they found that the counterions in the electrolyte generally were placed unphysically close to the metal surface. This was a result of nonoptimal parametrization of the ionic shape function, which is determined by the σ and $\tilde{\rho}_{el,cut}$ parameters.[2] A similar unphysical placement of counterions was reported by Steinmann et al.[17] in their solvated model of pyridine adsorbed on a Au (111) surface. However, for the SiC semiconductor, we found that the counterions were placed at a reasonable distance from the slab surface (Figure 4a) when using the same default parameters for σ and $\tilde{\rho}_{el,cut}$. The distance of the first peak of counterion concentration is ~2−3 Å from the surface, which physically is reasonable compared to explicit solvent simulations showing that counterions reside roughly ~3−5 Å from the surface.[58,59] In comparison, Gauthier et al. found
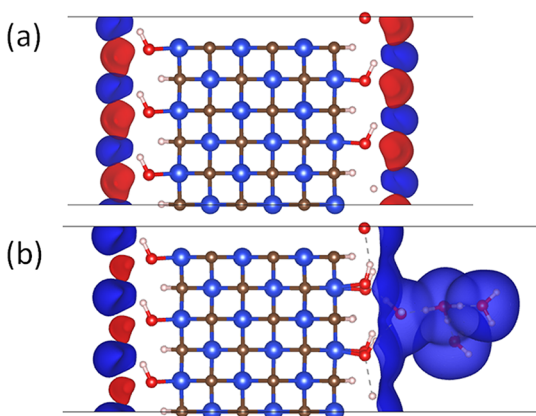
Figure 4. Ionic countercharge placement in the electrolyte surrounding the SiC (110) surface with a dissociated water layer at a surface charge density of 0 μC cm^{-2} (a) in the absence of an Eigen cation and (b) in the presence of an Eigen cation. An isovalue of 1 × 10^{-7} e Å^{-3} was used to generate both isosurfaces (blue: Si, brown: C, red: O, white: H, dashed lines: hydrogen bonds, red isosurface: cation, blue isosurface: anion).

charge placement within 2 Å of the Pt (111) surface. Also, the slab with an Eigen cation, which we use later for HER investigation, has a reasonable placement of counterions, as shown in Figure 4b. Here, the more realistic distance of counterions from SiC surface might be due to the presence of the dissociated water layer on the surface, where ions are separated from the surface by an effective hydration shell and physisorbed water.[2]

Counterions are assumed to be point charges in the VASPsol model, therefore, while modeling different electrode/electrolyte interfaces, a careful examination of the ionic countercharge placement, as presented here, is required and optimized model parameters should be selected. The artifact caused by the point charge assumption, while less severe for SiC compared to metal surfaces,[2,17] could be improved with other solvation models like charge-asymmetric nonlocally determined local-electric (CANDLE)[60] and effective screening method-reference interaction site method (EMS-RISM).[61]

We obtained the surface charge density profiles as a function of potential (σ_q vs ϕ) by sampling the electron chemical potentials at various surface charge densities on the SiC (110) surface covered with a dissociated water layer in the absence (Figure 5a) and presence (Figure 5b) of an Eigen cation. The surface charge density computation accounts for the area of both sides of the slab. The relationship between surface charge density and electrode potential has a similar trend with and without the added Eigen cation. The charge state and the work function of the electrode are determined by the electrode potential and are not affected by the Eigen cation. The Eigen cation only induces minor charge polarization at the electrode surface, which is screened by the water molecules of the Eigen cation and the dissociated water layer on the surface. The electrode potential of zero charge (PZC) corresponds to 0.02 V_{SHE} and 0.06 V_{SHE} with and without the Eigen cation, respectively. The curve to the right of the PZC reflects positive surface charge densities corresponding to variation in the occupation of the valence band. The curve to the left of the PZC represents negative surface charge densities corresponding to variation in the occupation of the conduction band. The discontinuity between the two curves at zero surface charge density represents the bandgap of the semiconductor, which
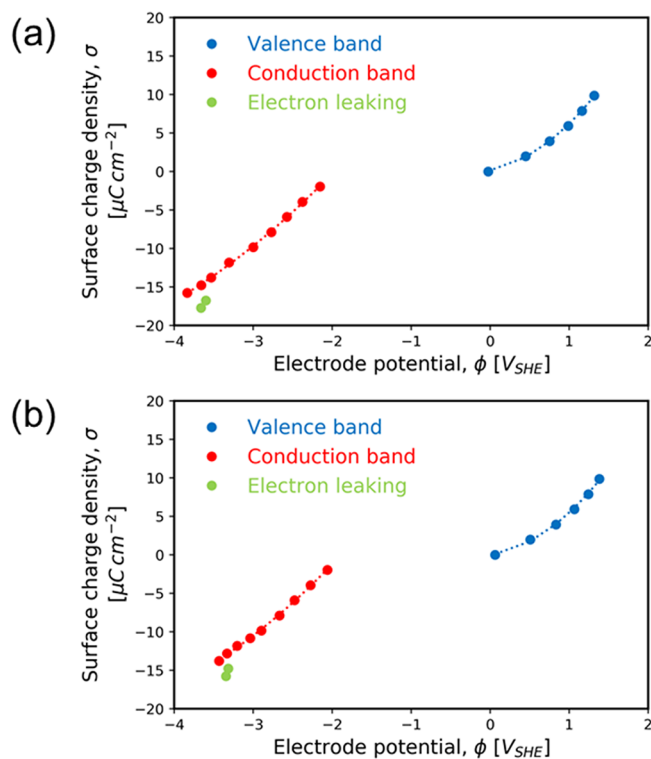
Figure 5. Potential versus surface charge density profiles of SiC (110) covered with a dissociated water layer (a) in the absence of an Eigen cation and (b) in the presence of an Eigen cation.

corresponds to a magnitude of ~1.86 eV. This energy gap is close to the fundamental bandgap of 2.15 eV computed with the PBE functional at zero charge density. These plots emphasize the semiconducting nature of the electrode surface, where electron chemical potentials inside the range of the bandgap are unattainable.

We note that band edge positions estimated from Figure 5a match closely to those shown in Figure 3a for SiC (110) surface models with implicit solvation (label I). The difference remains because a different method was used for the bandgap calculation (i.e., G_0W_0 versus PBE) in Figure 3a. For both valence band and conduction band data points in Figure 5, quadratic polynomials give a reasonable fit to this data with R^2 > 0.99. The curves on either side of the bandgap resemble the σ_q vs ϕ behavior of a metallic electrode because the Fermi level is shifting within the partially filled valence band or conduction band in these regions.[4] The slope of these curves ($\partial\sigma_q/\partial\phi$) yields the double-layer capacitance and the slope at the PZC yields the double-layer capacitance for the SiC (110) surface at 1 M concentration of electrolyte.[4] From these curves, we obtained the capacitance for the two systems at PZC as 2.31 and 1.95 μF cm^{-2}, respectively, which compare well with the experimental PZC capacitance for an n-type 3C-SiC of ~1.4 μF cm^{-2} at pH = 0.[62]

The data points at extremely negative potentials breaking the trend are artifacts from the well-described electron leaking phenomenon.[5] This occurs at large negative potentials when the electron density becomes so high on the surface that electrons from the surface "leak" into the electrolyte. We confirmed this electron leaking phenomenon by plotting isostructural charge density differences comparing differential changes in the electron density before and after the onset of the model's failure. These plots, shown in Figure S3 of the

Supporting Information, clearly show the charge density leaking into the electrolyte indicating that the model cannot be used to study such highly negative potentials. Thus, we restricted our analysis to potentials and surface charge densities that fall well before the onset of this physical artifact.

3.3. HER Mechanism on 3C-SiC (110). Having established the applicability of the VASPsol implicit solvation model for 3C-SiC, we next utilized it to investigate the mechanism of HER. The solvated SiC (110) surface is used for our study of the HER mechanism, which is covered with a dissociated water layer on both sides of the slab and has a cluster of four water molecules solvating a proton on one side of the slab, as shown in Figure 1c. This solvated surface model will be referred to simply as SiC (110) from here onward. The schematic of the reaction mechanism with density of states (DOS) and geometries of all the reaction intermediates are shown in Figures 6 and 7, respectively. In the following, H*
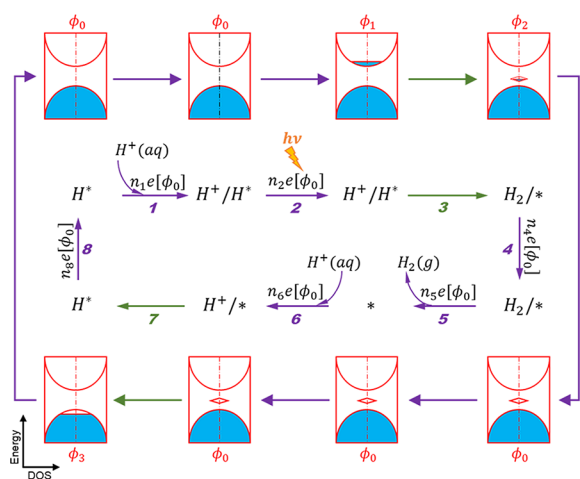
Figure 6. Illustration of the reaction mechanism (in the center) and the evolution of the density of states (DOS) (on the outside) of SiC (110) along the reaction path. The steps involved in the mechanism (described in the main text) are labeled below the arrows in the reaction mechanism. The arrows and the steps representing constant potential steps (1, 2, 4, 5, 6, and 8) and constant electron steps (3: Heyrovsky, 7: Volmer) are colored in purple and green, respectively. H* represents the hydrogen adsorbed on the C site of SiC surface, * represents a bare C site, H^+ represents a hydrogen ion that is part of Eigen cation in the simulation cell, $H^+(aq)$ represents a hydrogen ion that is present in the aqueous reservoir at 1 M concentration of H^+, H_2 represents hydrogen molecule formed in the simulation cell, $H_2(g)$ represents the hydrogen gas at 1 bar pressure, $e[\phi_0]$ represents the electron at the potential of the potentiostat (set at $\phi_0 = \phi_{VB}$) that is exchanged during a constant potential step, and the number of electrons exchanged are labeled as n_{step}. The blue color in the DOS represents filled states, which also represents the potential (ϕ) of the surface. The potentials (ϕ) of the SiC surface along the reaction path are labeled next to the DOS with red color. Structures of all the unique reaction intermediates involved in this mechanism are shown in Figure 7.

represents the hydrogen atom adsorbed on a C site of the surface, * represents a bare C site on the surface, H^+ represents a hydrogen ion that is part of Eigen cation in the simulation cell, $H^+(aq)$ represents a hydrogen ion that is present in the aqueous reservoir at 1 M concentration of H^+, H_2 represents hydrogen molecule formed in the simulation cell, $H_2(g)$ represents the hydrogen gas at 1 bar pressure, and $n_{step}e$ represents the number of electrons exchanged during a
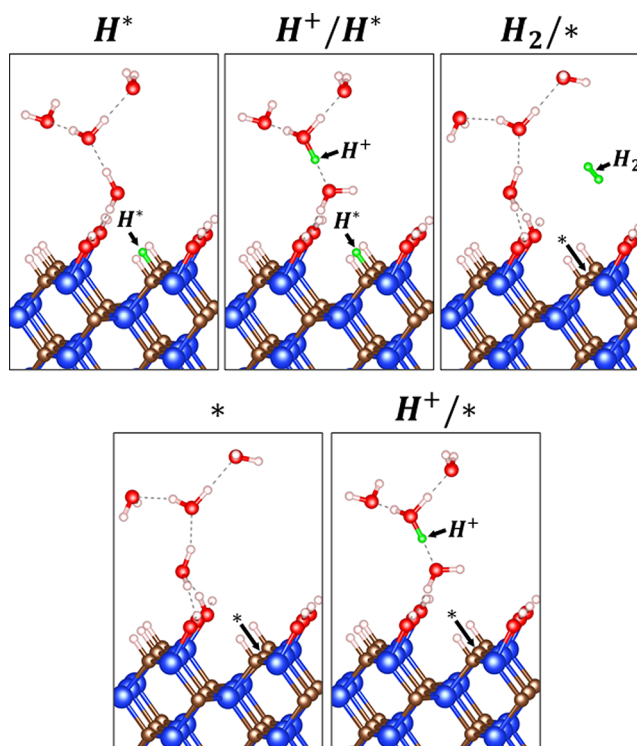
Figure 7. Structures of the unique reaction intermediates involved in the proposed HER mechanism presented in Figure 6. All the structures contain a SiC (110) surface covered with dissociated water and four explicit water molecules. H* represents the hydrogen adsorbed on the C site of SiC surface, * represents a bare C site, H^+ represents a hydrogen ion that is part of Eigen cation in the simulation cell, and H_2 represents hydrogen molecule formed in the simulation cell (blue: Si, brown: C, red: O, white: H, green: H atoms undergoing reaction, dashed lines: hydrogen bonds).
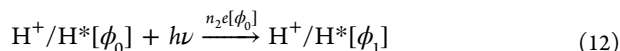
reaction step. ϕ_0 is the potential of the potentiostat that is fixed at the potential of the valence band edge (ϕ_{VB} = 0.06 V_{SHE}), which sets the chemical potential of all electrons added to or removed from the system over the course of the reaction cycle. ϕ_1 is the potential of the conduction band under photoexcitation and is determined by the surface charge density on the electrode. The terms ϕ_2 and ϕ_3 are the potentials of the electrode after the Heyrovsky (step 3) and Volmer (step 7) reactions, respectively. The chemical potentials of electrons in the electrode and $H^+_{(aq)}$ are calculated using eqs 8 and 9, respectively. Since the initial structure of SiC (110) is fully covered with dissociated water, we consider a model in which a Heyrovsky step generating H_2 precedes a Volmer step that regenerates the fully covered surface. A similar assumption was made by Shen et al.[37] when studying HER on SiC (111) and (100) surfaces that are fully covered with adsorbed hydrogen atoms. The elementary steps of our proposed HER mechanism along with the corresponding reaction energies are listed below in eqs 10−28.

Step 1. The first step of the mechanism describes the energy required to bring a bulk solvated proton from a reservoir at pH = 0 to the surface, which occurs at a constant potential by exchanging n_1 electrons with the potentiostat at ϕ_0.

$$H^+_{(aq)} + H^*[\phi_0] \xrightarrow{n_1 e[\phi_0]} H^+/H^*[\phi_0] \tag{10}$$
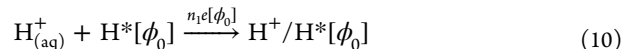
$$\Delta G_1 = G^{\phi_0}_{H^+/H^*} - G^{\phi_0}_{H^*} - \mu^0_{H^+} - n_1 \mu^{\phi_0}_e \tag{11}$$

Step 2. In the second step, electrons from the valence band are photoexcited to the conduction band at ϕ_1, leaving behind holes that are filled by the inflow of n_2 electrons from the potentiostat at ϕ_0. Both the electron chemical potential and surface charge density of SiC change during this step depending on the extent of photoexcitation. The electrode surface is assumed to be in constant equilibrium with incoming photons, meaning that this step has overall zero reaction free energy. The required energy and photon wavelength to excite the electron into the conduction band is calculated with eq 14.

$$H^+/H^*[\phi_0] + h\nu \xrightarrow{n_2 e[\phi_0]} H^+/H^*[\phi_1] \tag{12}$$

$$\Delta G_2 = G^{\phi_1}_{H^+/H^*} - G^{\phi_0}_{H^+/H^*} - n_2 \mu^{\phi_0}_e - h\nu = 0 \tag{13}$$

$$h\nu = G^{\phi_1}_{H^+/H^*} - G^{\phi_0}_{H^+/H^*} - n_2 \mu^{\phi_0}_e \tag{14}$$

Step 3. The Heyrovsky reaction occurs in the third step, when a H^+ from the electrolyte reacts with a H^* to form H_2 by withdrawing two electrons from the electrode. In an experimental system, the withdrawal of electrons does not change the Fermi level of the electrode or the electron chemical potential because the electrons are constantly replenished from the counter electrode through an external circuit to maintain a constant potential difference. Therefore, the electrode potential does not fluctuate during the reaction. However, in a simulated electrode, under the restriction of a neutral cell and a constant number of electrons, the transfer of electrons from SiC to H^+ while forming H_2 causes a large change in the surface charge density and a large shift in the Fermi level. On a metal electrode, this reaction can be modeled as a constant-potential step by injecting electrons to maintain a constant Fermi level because there is a continuous band of states.[13−18] However, on a semiconductor electrode, a similar constant-potential approach cannot be applied directly, as the Fermi level may shift between bands because of the discontinuity in available states. The change in the electron chemical potential depends on the change in surface charge density, which in turn depends on the size of the simulation cell[63] as discussed in detail in the following section. We note that the overall charge state of the entire simulation cell does not change during this step and therefore we call this a constant-electron step.

$$H^+/H^*[\phi_1] \rightarrow H_2/*[\phi_2] \tag{15}$$

$$\Delta G_3 = G^{\phi_2}_{H_2/*} - G^{\phi_1}_{H^+/H^*} \tag{16}$$

Step 4. The fourth step involves the equilibration of electrode potential to the applied potential. The electrode exchanges n_4 electrons with the potentiostat to reset the chemical potential of electrons to the valence band edge potential (ϕ_0).

$$H_2/*[\phi_2] \xrightarrow{n_4 e[\phi_0]} H_2/*[\phi_0] \tag{17}$$

$$\Delta G_4 = G^{\phi_0}_{H_2/*} - G^{\phi_2}_{H_2/*} - n_4 \mu^{\phi_0}_e \tag{18}$$

Step 5. In the fifth step, the H_2 molecule formed after the Heyrovsky reaction in step 3 is removed from the simulation cell representing the desorption of gas phase H_2 at standard conditions. This step occurs at a constant potential by exchanging n_5 electrons with the potentiostat at ϕ_0.

$$H_2/*[\phi_0] \xrightarrow{n_5 e[\phi_0]} *[\phi_0] + H_2(g) \tag{19}$$
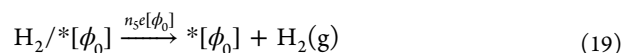
$$\Delta G_5 = \mu^0_{H_2} + G^{\phi_0}_* - G^{\phi_0}_{H_2/*} - n_5 \mu^{\phi_0}_e \tag{20}$$

Step 6. The sixth step is similar to step 1, where a second proton is added from the solvated proton reservoir at pH = 0 to the simulation cell to prepare the system for a Volmer reaction. This step occurs at a constant potential by exchanging n_6 electrons with the potentiostat at ϕ_0.

$$H^+_{(aq)} + *[\phi_0] \xrightarrow{n_6 e[\phi_0]} H^+/*[\phi_0] \tag{21}$$
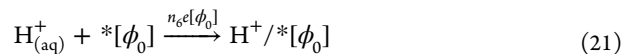
$$\Delta G_6 = G^{\phi_0}_{H^+/*} - G^{\phi_0}_* - \mu^0_{H^+} - n_6 \mu^{\phi_0}_e \tag{22}$$

Step 7. The Volmer reaction occurs next, where an H^+ from the electrolyte refills the vacancy on the C site created during the Heyrovsky step, restoring the initial surface structure. This step, like the Heyrovsky step, is also treated as a constant-electron step.

$$H^+/*[\phi_0] \rightarrow H^*[\phi_3] \tag{23}$$
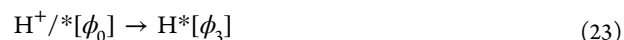
$$\Delta G_7 = G^{\phi_3}_{H^*} - G^{\phi_0}_{H^+/*} \tag{24}$$

Step 8. Finally, the chemical potential of the electrons is equilibrated to the valence band edge by exchanging n_8 electrons with the potentiostat. This restores the state of the system and completes the thermodynamic reaction cycle.

$$H^*[\phi_3] \xrightarrow{n_8 e[\phi_0]} H^*[\phi_0] \tag{25}$$

$$\Delta G_8 = G^{\phi_0}_{H^*} - G^{\phi_3}_{H^*} - n_8 \mu^{\phi_0}_e \tag{26}$$

Overall Reaction. The overall reaction energy obtained from steps 1−8 is equal to the HER reaction energy computed at a fixed applied potential of ϕ_0 plus the additional $h\nu$ supplied by photoexcitation.

$$2H^+_{(aq)} + h\nu \xrightarrow{(n_1+n_2+n_4+n_5+n_6+n_8)e[\phi_0]} H_2(g) \tag{27}$$
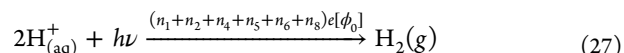
$$\Delta G_{overall} = \mu^0_{H_2} - 2\mu^0_{H^+} - (n_1 + n_2 + n_4 + n_5 + n_6 + n_8)$$
$$\mu^{\phi_0}_e - h\nu \tag{28}$$

An alternative to the Heyrovsky reaction is the Tafel reaction, which occurs when two adjacently adsorbed hydrogen atoms react to form H_2. The adjacent C sites holding the H atoms on the SiC (110) surface are separated by a large distance of ~3.1 Å, so we believe that the Tafel reaction would be kinetically hindered on this surface and do not consider this step further.

We modeled the steps proposed in the reaction mechanism by determining the respective electron chemical potentials and free energies of all the reaction intermediates at varying potentials controlled with the iterative canonical SCF approach described earlier. We find that quadradic polynomial functions best describe the relations between the surface charge densities, chemical potentials, and free energies for all the reaction intermediates. The chemical potential and free energy data for all the surface intermediates, along with the regressed quadratic relations and their R^2 values are included in Figures S8−S13 of the Supporting Information. Most of the R^2 values are greater than 0.99. Using these relations, we can determine the free energies of all the reaction intermediates at any given

potential and thereby the reaction energies of all the steps as a function of potential using eqs 10−28.

3.4. Dependence of Reaction Energetics on the Surface Charge Density for Constant-Electron Reactions. Since the Heyrovsky and Volmer steps of the reaction mechanism are modeled as constant-electron steps, their reaction energies can be determined directly from the differences in the energies of their initial (IS) and final (FS) states, which have the same number of electrons. As such, we can scan the reaction energies over varying numbers of electrons in the IS or FS (i.e., over a range of surface charge densities). Figure 8a shows the energies of the IS and FS for
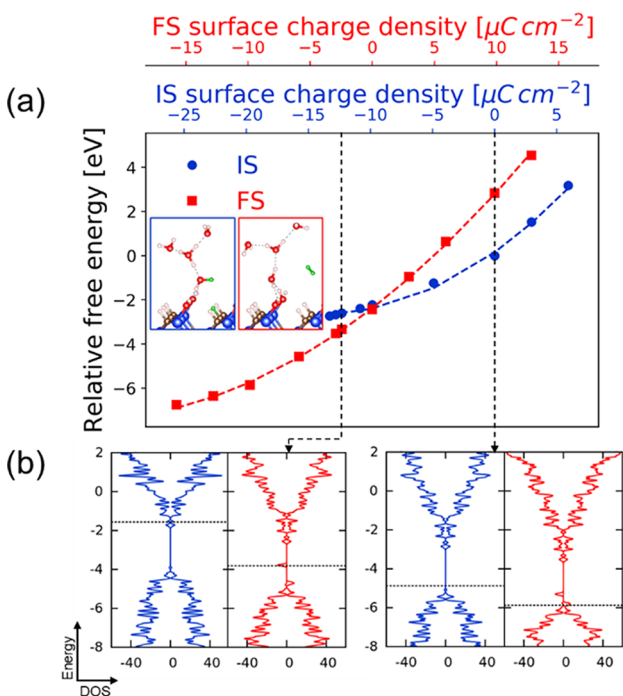
Figure 8. (a) Relative free energies of the initial (IS) and final (FS) states of the Heyrovsky reaction plotted against surface charge density on a (3 × 2) SiC (110) surface. A vertical line on this plot represents the reaction energy of a constant-electron Heyrovsky step. All the energies are plotted relative to the energy of the IS with a surface charge density of 0 μC cm^{-2}. (inset) Geometries of the IS and FS. (b) DOS of the IS and FS for a constant-electron Heyrovsky reaction with IS surface charge densities 0 and −12.3 μC cm^{-2}. The DOS energies on the vertical axis are referenced to the bulk electrolyte, and the DOS on the horizontal axis has units of states eV^{-1} cell^{-1}. The black dotted line in the DOS represents the Fermi level.

the Heyrovsky reaction on the 3 × 2 SiC (110) surface. The separation of these energies along a vertical line on this figure yields the reaction energy for the Heyrovsky step in a constant-electron formalism. The surface charge densities of the IS and FS (on the x-axis) for a constant-electron Heyrovsky reaction are different because the formation of the H_2 molecule during the reaction requires the withdrawal of two electrons from the surface as they combine with the incoming proton. Thus, the size of the SiC simulation cell determines the change in the surface charge density from the IS to FS and thereby the change in the electron chemical potential during this reaction.[63] The magnitude of change in the surface charge density from the IS to FS (9.85 μC cm^{-2}) is quite high because of the small size of the 3 × 2 SiC (110) surface. Later, we show that this change is reduced when employing larger surface

models, as the change in number of electrons over the course of the reaction remains the same but is spread over a wider area. Finally, the surface charge densities calculated here for the SiC (110) surface are similar to those reported in previous literature for the Pt (111) surface (∼10 μC cm^{-2}) at similar electrode potentials.[5] In addition, the double layer capacitance for 3C-SiC reported by Zhuang et al.[64] from the cyclic voltammetry experiments is in the range of 40−70 μF cm^{-2} at the operating potentials of 0−0.8 V. A calculation for surface charge density from these values, using a parallel-plate capacitor model ($Q = CV$), would result in the surface charge densities in the range of 0−60 μC cm^{-2}. This range of surface charge densities calculated here is just an estimate and would depend on several factors related to the characteristics of surface, electrolyte, and other experimental parameters. Nevertheless, the surface charge densities sampled in our work fall in this estimated range of surface charge densities at plausible experimental conditions.

As expected, the reaction is less favorable when the surface is more positively charged. Accordingly, the reaction energy decreases under more negative surface charge densities, implying that higher electron densities, driven by photo-excitation, make the Heyrovsky reaction more favorable on the SiC surface. When decreasing the surface charge density, the slope of the IS energy curve decreases more rapidly compared to that of the FS, causing the reaction to become exothermic beyond the intersection point of the two curves. As shown in the inset of Figure 8a, the FS has a H vacancy on the C site. The addition of electrons stabilizes the FS surface by saturating the dangling bond of the surface C site. Therefore, the addition of electrons is more favorable in the FS compared to the fully saturated IS, as evident from the slopes in Figure 8a. This is confirmed from the DOS plots of the IS and FS shown in Figure 8b at two different charge states (marked by vertical lines in Figure 8a). Extra electrons in the IS are added to the conduction band (higher in energy), while in the FS they are added to the midgap state of the undercoordinated C atom (lower in energy). Therefore, the addition of electrons in the FS comes at a lower energetic cost compared to the IS. We confirm that the midgap state corresponds to the H vacancy on the C site by imaging this state as shown in Figure S5 of the Supporting Information.

Because of the shortcomings of PBE in dealing with electron self-interaction and overestimation of electron delocalization,[65] we performed test calculations for the two surface charge densities using more accurate SCAN[41] and HSE06[42] exchange-correlational functionals. SCAN is a nonempirical meta-generalized gradient approximation (GGA) functional that gives a better description of covalent bonding, bandgaps, and electron delocalization but is still prone to electron self-interaction error.[66] HSE06 is a hybrid functional that reduces the electron self-interaction error by including a portion of exact exchange energy but is computationally more expensive. Therefore, we compare these functionals against PBE by performing full geometry optimizations with SCAN and only single-point electronic optimizations with HSE06. We find that the energies of the IS and FS do not change significantly using these functionals (Figure S5 in the Supporting Information). Also, the DOS and electron density localization of the midgap states of the FS are very similar for the three functionals (Figure S5 in the Supporting Information), implying that the band diagrams and extent of electron delocalization in this system are not affected by the choice of the functional.

The variation of transition state (TS) energies with changing surface charge density is also provided in Figure S6 of the Supporting Information. The energy curve of the TS has a trend and slope similar to that of the FS at all surface charge densities. The TS also has a similar midgap state compared to the FS (Figure S10 of the Supporting Information). This late transition state structure implies that, like the reaction energy, the activation energy of the Heyrovsky step would also decrease as the surface becomes more negatively charged, as expected from the well-known Brønsted−Evans−Polanyi (BEP) relation.[67,68]

Since the change in the surface charge density and electron chemical potential during the Heyrovsky reaction are dependent on the size of the simulation cell,[63] we studied the reaction energetics for different cell sizes. The energies of the IS and FS for the Heyrovsky reaction in larger cells, (3×4) and (6×4), are shown in Figures 9a and 10a, respectively. As the cell size
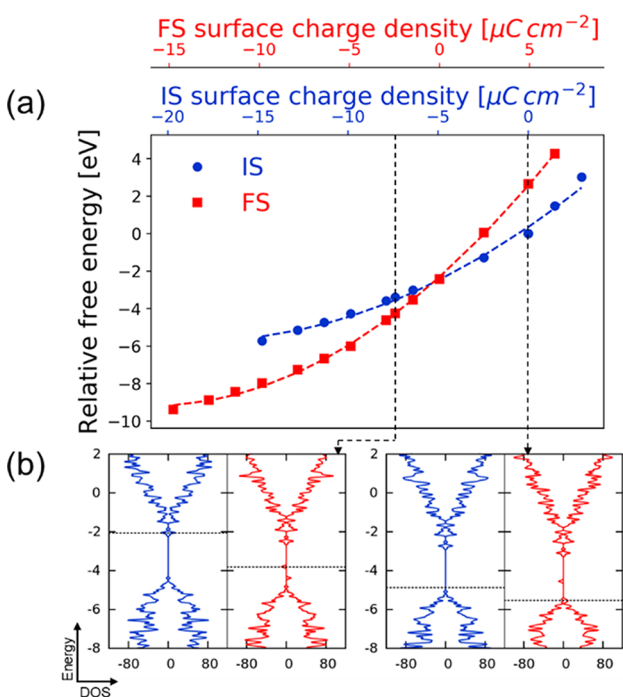
Figure 9. (a) Relative free energies of the initial (IS) and final (FS) states of the Heyrovsky reaction plotted against the surface charge density on a (3×4) SiC (110) surface. A vertical line on this plot represents the reaction energy of a constant-electron Heyrovsky step. All the energies are plotted relative to the energy of the IS with a surface charge density of 0 μC cm^{-2}. (b) DOS of the IS and FS for a constant-electron Heyrovsky reaction with IS surface charge densities 0 and −7.4 μC cm^{-2}. The DOS energies on the vertical axis are referenced to the bulk electrolyte, and the DOS on the horizontal axis has units of states eV^{-1} cell^{-1}. The black dotted line in the DOS represents the Fermi level.
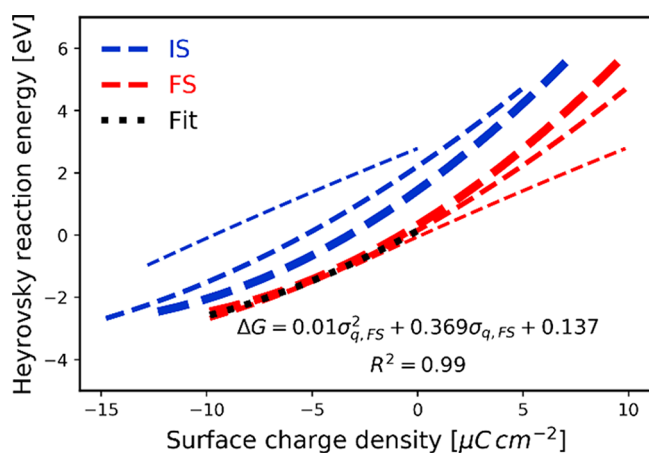
increases, the change in the surface charge density from IS to FS during a constant-electron Heyrovsky reaction decreases (i.e., as evident from the relative position of surface charge density axes). The resulting change in the electrode potential during the reaction also decreases, and in the limit of a very-large simulation cell, the surface charge density and electrode potential would remain unchanged. The reduced change in the surface charge density occurs because the surface loses two electrons to form a hydrogen molecule irrespective of the size of the simulation cell. This means that for the same IS surface
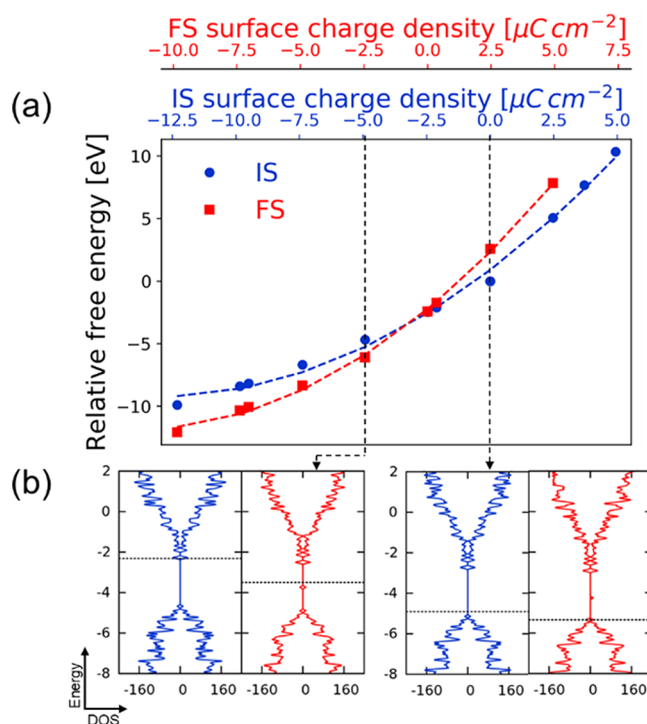
Figure 10. (a) Relative free energies of the initial (IS) and final (FS) states of the Heyrovsky reaction plotted against the surface charge density on a (6×4) SiC (110) surface. A vertical line on this plot represents the reaction energy of a constant-electron Heyrovsky step. All the energies are plotted relative to the energy of the IS with a surface charge density of 0 μC cm^{-2}. (b) DOS of the IS and FS for a constant-electron Heyrovsky reaction with IS surface charge densities 0 and −4.9 μC cm^{-2}. The DOS energies on the vertical axis are referenced to the bulk electrolyte, and the DOS on the horizontal axis has units of states eV^{-1} cell^{-1}. The black dotted line in the DOS represents the Fermi level.

charge density, the reaction would become more favorable in a larger surface cell as the FS surface would be more negatively charged, making the undercoordinated surface C more stable. As expected, the favorability of the reaction depends on the stability of the FS. The reaction becomes more exothermic as the surface becomes more negatively charged in the FS. This suggests that FS surface charge density is a better descriptor of reaction energy than the IS surface charge density.

We plot the Heyrovsky reaction energies as functions of the IS and FS surface charge densities for different cell sizes, as shown in Figure 11. The reaction energies vary significantly with the size of the simulation cell for the same IS surface charge density but remain relatively unchanged with respect to the simulation cell size for the FS surface charge density, especially in the physically relevant range of surface charge densities (0 to −10 μC cm^{-2}). It is also evident from the figure that the difference in the IS and FS surface charge densities for the same reaction energy (obtained by following a horizontal line from the IS curve to the FS curve) decreases as the surface cell size increases, as expected. In the limit of a very-large simulation cell, the IS and FS curves of reaction energies would merge. Since the reaction energies are independent of the size of the FS simulation cell, they can be determined in the infinite limit as a function of FS surface charge densities. Here, we used a regression on the reaction energy data from the FS simulation cells of three sizes to determine a quadratic

Figure 11. Reaction energies of the Heyrovsky reaction at various surface charge densities of the initial (IS) and final (FS) states. The thickness of curves represents the size of the surface cells where increasing thickness corresponds to increased cell size: $(3 \times 2) < (3 \times 4) < (6 \times 4)$. The relation between the reaction energy and surface charge density is determined by fitting a quadratic polynomial on the data of reaction energies for the three surfaces with the FS charge density ranging from 0 to -10 μC cm^{-2}.

relationship between reaction energy and FS surface charge density, i.e.,

$$\Delta G_{rxn} = 0.01\sigma_{q,FS}^2 + 0.369\sigma_{q,FS} + 0.137 \quad (R^2 = 0.99)$$

$$(29)$$

where $\sigma_{q,FS}$ is the surface charge density of the FS in units of μC cm^{-2} and ΔG_{rxn} is the free energy of the reaction in units of eV.

The dependence of Heyrovsky reaction energies on the FS surface charge densities is further established from the perspective of Fermi level in the DOS of the IS and FS in Figure 12. We plot the DOS of the IS and FS on (3×2), (3×4), and (6×4) surfaces with charge densities yielding the same reaction energy of -0.7 eV. These reaction energies correspond to the left vertical lines marked on Figures 8a, 9a, and 10a. The figure shows that, for a given reaction energy, the Fermi level of the FS does not change much compared to that of IS for various surfaces, meaning that the reaction free energy has greater dependence on the Fermi level of the FS. Also, since the position of the FS Fermi level determines the electron chemical potential, the surface charge density, and the stability of the FS, we can conclude that the reaction energy of the Heyrovsky step depends on the chemical potential, surface charge density, and stability of the FS. The respective IS Fermi levels have to be adjusted by varying the surface charge to achieve the same FS Fermi level on differently sized simulation cells, as shown in Figure 12, giving rise to the dependence of the reaction energy on the IS simulation cell size.

From Figure 11, we see that the dependence of the Heyrovsky reaction free energies on FS surface charge density is generally valid in a certain range (0 to -10 μC cm^{-2}) and deviates at positive surface charge densities. For surface charge densities in the range of 0 to -10 μC cm^{-2}, the Fermi level generally lies in the midgap state of the FS, which has a single electronic state corresponding to the H vacancy created on the C site of the surface. Since different-sized simulation cells have the same number of midgap states, the Fermi level does not change much as a function of cell size and the dependence of
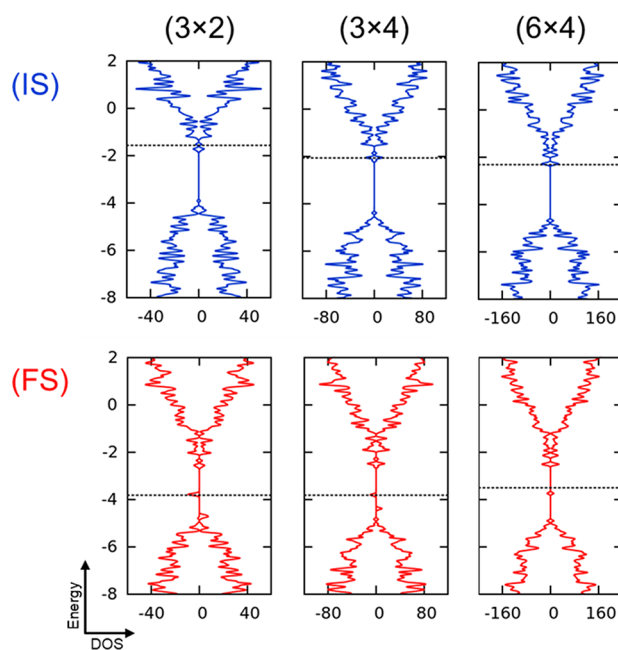
Figure 12. Comparison of Fermi levels in the density of states (DOS) of the initial (IS) and final (FS) states of the Heyrovsky reaction on (3×2), (3×4), and (6×4) surfaces for similar reaction free energies near -0.7 eV. The DOS energies on the vertical axis are referenced to the bulk electrolyte, and the DOS on the horizontal axis has units of states^{-1} eV^{-1} cell^{-1}. The black dotted line in the DOS represents the Fermi level.

the reaction energy on the FS Fermi level holds. On the other hand, for very positive surface charge densities, the Fermi level generally would lie in the valence band and its position would be influenced by the cell size. This also explains the differences in the Heyrovsky reaction energies at the same IS surface charge densities on different surfaces. The IS Fermi level usually would lie in the conduction band, where its position, as shown in Figure 12, would be influenced by the difference in the number of states available in differently sized simulation cells. Similarly, we plotted the activation energies of the Heyrovsky reaction for the IS and TS surface charge densities (shown in Figure S7 of the Supporting Information). As discussed earlier, the TS has a similar energy trend as the FS over the entire range of surface charge density and has a similar midgap state. Therefore, the activation energy trends (Figure S7) are similar to those found for the reaction energies (Figure 11), meaning that the activation energies are determined by the TS surface charge densities. Therefore, activation barriers can be determined in the limit of a large simulation cell using the surface charge density of the TS surface. We propose that this framework would apply to a variety of photoelectrochemical reactions in which the final state or the transition state results in a midgap electronic state attained by the loss (gain) of electrons from (to) the conduction band (valence band) of the initial state of the reaction.

The energies of the IS and FS of the Volmer reaction on a (3×2) SiC (110) surface are shown in Figure 13a. The Volmer reaction is highly favorable and is exothermic even for negligible charge density on SiC (110) surface. Moreover, since the dissociative adsorption of water on SiC (110) is quite favorable,[48] the spontaneous nature of the reaction of a hydronium cation with a bare C site is not surprising. Furthermore, on metal electrodes the variation in electrode
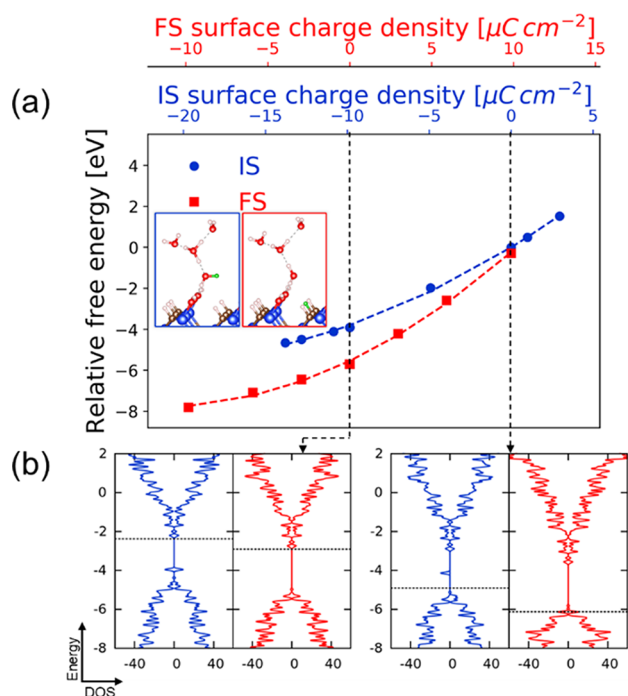
Figure 13. (a) Relative free energies of the initial (IS) and final (FS) states of the Volmer reaction plotted against the surface charge density on a (3×2) SiC (110) surface. A vertical line on this plot represents the reaction energy of a constant-electron Volmer step. All the energies are plotted relative to the energy of the IS with a surface charge density of $0 \ \mu C \ cm^{-2}$. (inset) Geometries of the IS and FS. (b) DOS of the IS and FS for a constant-electron Volmer reaction with IS surface charge densities of 0 and $-9.9 \ \mu C \ cm^{-2}$. The DOS energies on the vertical axis are referenced to the bulk electrolyte, and the DOS on the horizontal axis has units of states $eV^{-1} \ cell^{-1}$. The black dotted line in the DOS represents the Fermi level.

Figure 14. Reaction energy diagram of HER on the 3C-SiC (110) surface at different surface charge densities (σ_q, in units of $\mu C \ cm^{-2}$) of the final state of the Heyrovsky step. The wavelengths of the incident photons (λ) required to achieve these surface charge densities in the final state are also shown. (inset) Initial (IS), transition (TS), and final (FS) states of the Heyrovsky reaction at σ_q = 0 $\mu C \ cm^{-2}$ (blue: Si, brown: C, red: O, white: H, green: H atoms undergoing reaction, dashed lines: hydrogen bonds, dotted lines: TS bonds).

potential changes the hydrogen coverage because water dissociation typically is not spontaneous.[69] However, on SiC electrodes, it has been shown experimentally that the hydrogen coverage does not change throughout the reaction and is independent of the applied potential.[70] This relates well with our results, which suggests that for a wide range of surface charge density (i.e., electrode potential) the Volmer reaction would occur readily to maintain the surface hydrogen coverage.

3.5. Overall Reaction Energy Diagram of HER on 3C-SiC (110). The Volmer reaction occurs spontaneously on SiC(110), so we focus here primarily on the Heyrovsky reaction. Since the Heyrovsky reaction energy depends on the surface charge density of the FS surface, and the path of the reaction is unique for a given surface charge density, we can determine the reaction energy diagrams as a function of these FS surface charge densities. Here, we have sampled the reaction energy diagrams corresponding to three different FS surface charge densities (0, -1, and $-2 \ \mu C \ cm^{-2}$) of the Heyrovsky reaction (Figure 14). The structures of the IS, TS, and FS of the Heyrovsky reaction for the FS surface charge density of $0 \ \mu C \ cm^{-2}$ are shown in the inset of Figure 14. Reaction data for the electron chemical potential, number of electrons, and energy of all reaction intermediates for the three FS surface charge densities are provided in Tables S1–S3 of the Supporting Information. For each of the three surface charge densities, a total of two electrons are consumed in the overall reaction and the reaction energies computed without

the contribution from the variable photon energy is the same, as expected (i.e., $2e\phi_{VB} = 2 \times 0.06 \ eV = 0.12 \ eV$).

The Heyrovsky step is rate-determining for HER over the SiC (110) surface. All other steps are downhill in energy and the overall reaction is exothermic because of the energy supplied by illumination. The surface charge density of the FS in the Heyrovsky reaction is determined by the extent of photoexcitation in step 2 of the reaction mechanism. More photoexcitation would result in more negative surface charge densities in the IS and FS of the Heyrovsky reaction, making the reaction more favorable as shown in Figure 14. With increasing charge density, the reaction energy decreases from -0.1 to $-0.7 \ eV$, and the activation energies follow a similar trend, decreasing from 0.91 to 0.42 eV. Activation barriers of $\sim 0.4 \ eV$ are surmountable with the thermal energy available at room temperature.[71,72] After the Heyrovsky reaction, the chemical potential of the surface electrons is restored to the valence band chemical potential by the potentiostat at ϕ_0 in step 4. This, in turn, restores the surface charge density to the same initial value irrespective of the surface charge density of the FS of the Heyrovsky reaction. Therefore, the reaction energies of all remaining steps of the mechanism do not change with respect to the surface charge density during the Heyrovsky step.

These results are in good agreement with experiments by He et al.[24] showing that illumination enhances HER activity on SiC. For the photoexcitation step of the reaction mechanism, we calculated the wavelength of the photons by considering a 1:1 ratio of photons to excited electrons. This consideration assumes an ideal system where the change in the energy of the electron is equal to the energy of the incident photon, which could be affected by other phenomena (e.g., doping, band bending, light absorption, carrier mobility, recombination, etc.) specific to the experimental system. Hence, the computed wavelengths are just an estimate. The calculated wavelengths are in the visible spectrum, which combined with surmount-

able activation barriers for the Heyrovsky step, confirm the feasibility of a self-driven photo-electrochemical HER over SiC, as was demonstrated in previous experiments.[23] Moreover, the magnitude of the calculated wavelength (515 nm) compares well with the experimental wavelength of ~520 nm for solar water splitting on 3C-SiC.[25]

4. CONCLUSION

We utilized an implicit solvation model in conjunction with DFT to develop a framework for studying the HER mechanism over 3C-SiC (110) under constant applied potential and illumination. We find that the Heyrovsky step is the rate-limiting step and its reaction energy and activation energy depend on this step's final surface charge density irrespective of the simulation cell size. The Heyrovsky reaction energy and barrier can be lowered by stabilizing the final state by increasing the negative surface charge density through higher degrees of photoexcitation. We determine that a photon wavelength of 515 nm lowers the barrier so that it is surmountable at room temperature, supporting the feasibility of HER over SiC under visible light.

The methodology developed in this work can be utilized as a general tool for investigating a range of photo-electrochemical reaction mechanisms on solvated semiconductor surfaces. The implementation of electronic grand canonical formalism on these experimentally relevant periodic surfaces provides a more accurate route for determining how the favorability of a reaction is influenced by the explicit surface charge state. This is valuable for exploring ways in which electrochemical reactions can be controlled by tailoring the behavior of the surface charge by introducing surface modifications in the form of dopants or cocatalysts. For example, recent computational studies have demonstrated such strategies for engineering semiconductor surfaces with electron-donating and electron-withdrawing dopants and cocatalysts to tune reaction energetics for CO_2 reduction.[73,74] The methods developed here can be utilized to evaluate how explicit surface charge interacts with the surface modifications (e.g., charge localization at dopant sites). This can help expedite the experimental exploration toward designing effective photocatalysts.

ASSOCIATED CONTENT

Ⓢ Supporting Information

The Supporting Information is available free of charge at https://pubs.acs.org/doi/10.1021/acs.jpcc.0c07583.

> VASPsol implicit solvation model equations and discussion of the electron leaking phenomenon. Verification of certain reaction energies, DOS, and imaging of midgap states using HSE06 and SCAN functionals. Activation barriers of the HER Heyrovsky step as a function of surface charge density. Details of potentials, charge transfer, and reaction energies for each mechanism step at varying surface charge densities. Plots of the potentials and energies of all reactions intermediates as a function of surface charge density, along with the regressed polynomial relationship and R^2 (PDF)

AUTHOR INFORMATION

Corresponding Author

Thomas P. Senftle − *Department of Chemical and Biomolecular Engineering, Rice University, Houston, Texas 77005-1892, United States;* ⓞ orcid.org/0000-0002-5889-5009; Phone: +1-713-348-4714; Email: tsenftle@rice.edu

Authors

Manav Bhati − *Department of Chemical and Biomolecular Engineering, Rice University, Houston, Texas 77005-1892, United States*

Yu Chen − *Department of Chemical and Biomolecular Engineering, Rice University, Houston, Texas 77005-1892, United States*

Complete contact information is available at:
https://pubs.acs.org/10.1021/acs.jpcc.0c07583

Author Contributions

[†]M.B. and Y.C. contributed equally to this work.

Notes

The authors declare no competing financial interest.
All geometries and input files for the simulations are available at: https://github.com/tsenftle/PEC-Semiconductors.

REFERENCES

(1) Govind Rajan, A.; Martirez, J. M. P.; Carter, E. A. Why Do We Use the Materials and Operating Conditions We Use for Heterogeneous (Photo)Electrochemical Water Splitting? *ACS Catal.* **2020**, *10* (19), 11177−11234.

(2) Gauthier, J. A.; Ringe, S.; Dickens, C. F.; Garza, A. J.; Bell, A. T.; Head-Gordon, M.; Nørskov, J. K.; Chan, K. Challenges in Modeling Electrochemical Reaction Energetics with Polarizable Continuum Models. *ACS Catal.* **2019**, *9* (2), 920−931.

(3) Jinnouchi, R.; Anderson, A. B. Electronic Structure Calculations of Liquid-Solid Interfaces: Combination of Density Functional Theory and Modified Poisson-Boltzmann Theory. *Phys. Rev. B: Condens. Matter Mater. Phys.* **2008**, *77* (24), 245417.

(4) Mathew, K.; Sundararaman, R.; Letchworth-Weaver, K.; Arias, T. A.; Hennig, R. G. Implicit Solvation Model for Density-Functional Study of Nanocrystal Surfaces and Reaction Pathways. *J. Chem. Phys.* **2014**, *140* (8), 084106.

(5) Mathew, K.; Kolluru, V. S. C.; Mula, S.; Steinmann, S. N.; Hennig, R. G. Implicit Self-Consistent Electrolyte Model in Plane-Wave Density-Functional Theory. *J. Chem. Phys.* **2019**, *151* (23), 234101.

(6) Ikeshoji, T.; Otani, M. Toward Full Simulation of the Electrochemical Oxygen Reduction Reaction on Pt Using First-Principles and Kinetic Calculations. *Phys. Chem. Chem. Phys.* **2017**, *19* (6), 4447−4453.

(7) Cheng, T.; Xiao, H.; Goddard, W. A. Full Atomistic Reaction Mechanism with Kinetics for CO Reduction on Cu(100) from Ab Initio Molecular Dynamics Free-Energy Calculations at 298 K. *Proc. Natl. Acad. Sci. U. S. A.* **2017**, *114* (8), 1795−1800.

(8) Cheng, T.; Xiao, H.; Goddard, W. A. Free-Energy Barriers and Reaction Mechanisms for the Electrochemical Reduction of CO on the Cu(100) Surface, Including Multiple Layers of Explicit Solvent at pH 0. *J. Phys. Chem. Lett.* **2015**, *6* (23), 4767−4773.

(9) Holmberg, N.; Laasonen, K. Ab Initio Electrochemistry: Exploring the Hydrogen Evolution Reaction on Carbon Nanotubes. *J. Phys. Chem. C* **2015**, *119* (28), 16166−16178.

(10) Melander, M. M.; Kuisma, M. J.; Christensen, T. E. K.; Honkala, K. Grand-Canonical Approach to Density Functional Theory of Electrocatalytic Systems: Thermodynamics of Solid-Liquid Interfaces at Constant Ion and Electrode Potentials. *J. Chem. Phys.* **2019**, *150* (4), 041706.

(11) Kresse, G.; Furthmüller, J. Efficient Iterative Schemes for Ab Initio Total-Energy Calculations Using a Plane-Wave Basis Set. *Phys. Rev. B: Condens. Matter Mater. Phys.* **1996**, *54* (16), 11169−11186.

(12) Kresse, G.; Furthmüller, J. Efficiency of Ab-Initio Total Energy Calculations for Metals and Semiconductors Using a Plane-Wave Basis Set. *Comput. Mater. Sci.* **1996**, *6* (1), 15−50.

(13) Lindgren, P.; Kastlunger, G.; Peterson, A. A. A Challenge to the G ∼ 0 Interpretation of Hydrogen Evolution. *ACS Catal.* **2020**, *10* (1), 121−128.

(14) Van den Bossche, M.; Skúlason, E.; Rose-Petruck, C.; Jónsson, H. Assessment of Constant-Potential Implicit Solvation Calculations of Electrochemical Energy Barriers for H2 Evolution on Pt. *J. Phys. Chem. C* **2019**, *123* (7), 4116−4124.

(15) Ping, Y.; Nielsen, R. J.; Goddard, W. A. The Reaction Mechanism with Free Energy Barriers at Constant Potentials for the Oxygen Evolution Reaction at the IrO2 (110)Surface. *J. Am. Chem. Soc.* **2017**, *139* (1), 149−155.

(16) Xiao, H.; Cheng, T.; Goddard, W. A.; Sundararaman, R. Mechanistic Explanation of the PH Dependence and Onset Potentials for Hydrocarbon Products from Electrochemical Reduction of CO on Cu (111). *J. Am. Chem. Soc.* **2016**, *138* (2), 483−486.

(17) Steinmann, S. N.; Sautet, P. Assessing a First-Principles Model of an Electrochemical Interface by Comparison with Experiment. *J. Phys. Chem. C* **2016**, *120* (10), 5619−5623.

(18) Goodpaster, J. D.; Bell, A. T.; Head-Gordon, M. Identification of Possible Pathways for C-C Bond Formation during Electrochemical Reduction of CO2: New Theoretical Insights from an Improved Electrochemical Model. *J. Phys. Chem. Lett.* **2016**, *7* (8), 1471−1477.

(19) Chan, K.; Nørskov, J. K. Electrochemical Barriers Made Simple. *J. Phys. Chem. Lett.* **2015**, *6* (14), 2663−2668.

(20) Chan, K.; Nørskov, J. K. Potential Dependence of Electrochemical Barriers from Ab Initio Calculations. *J. Phys. Chem. Lett.* **2016**, *7* (9), 1686−1690.

(21) Walter, M. G.; Warren, E. L.; McKone, J. R.; Boettcher, S. W.; Mi, Q.; Santori, E. A.; Lewis, N. S. Solar Water Splitting Cells. *Chem. Rev.* **2010**, *110* (11), 6446−6473.

(22) Ros, C.; Andreu, T.; Morante, J. R. Photoelectrochemical Water Splitting: A Road from Stable Metal Oxides to Protected Thin Film Solar Cells. *J. Mater. Chem. A* **2020**, *8* (21), 10625−10669.

(23) Yasuda, T.; Kato, M.; Ichimura, M.; Hatayama, T. SiC Photoelectrodes for a Self-Driven Water-Splitting Cell. *Appl. Phys. Lett.* **2012**, *101* (5), 053902.

(24) He, C.; Wu, X.; Shen, J.; Chu, P. K. High-Efficiency Electrochemical Hydrogen Evolution Based on Surface Autocatalytic Effect of Ultrathin 3C-SiC Nanocrystals. *Nano Lett.* **2012**, *12* (3), 1545−1548.

(25) Jian, J.; Sun, J. A Review of Recent Progress on Silicon Carbide for Photoelectrochemical Water Splitting. *Sol. RRL* **2020**, *4* (7), 2000111.

(26) Ichikawa, N.; Kato, M.; Ichimura, M. The Enhanced Performance of 3C-SiC Photocathodes for the Generation of Hydrogen through the Use of Cocatalysts. *Appl. Phys. Lett.* **2016**, *109* (15), 153904.

(27) Li, B.; Jian, J.; Chen, J.; Yu, X.; Sun, J. Nanoporous 6H-SiC Photoanodes with a Conformal Coating of Ni-FeOOH Nanorods for Zero-Onset-Potential Water Splitting. *ACS Appl. Mater. Interfaces* **2020**, *12* (6), 7038−7046.

(28) Hao, J.-Y.; Wang, Y.-Y.; Tong, X.-L.; Jin, G.-Q.; Guo, X.-Y. Photocatalytic Hydrogen Production over Modified SiC Nanowires under Visible Light Irradiation. *Int. J. Hydrogen Energy* **2012**, *37* (20), 15038−15044.

(29) Wang, Y.; Guo, X.; Dong, L.; Jin, G.; Wang, Y.; Guo, X.-Y. Enhanced Photocatalytic Performance of Chemically Bonded SiC-Graphene Composites for Visible-Light-Driven Overall Water Splitting. *Int. J. Hydrogen Energy* **2013**, *38* (29), 12733−12738.

(30) Peng, K.; Zhou, J.; Gao, H.; Wang, J.; Wang, H.; Su, L.; Wan, P. Emerging One-/Two-Dimensional Heteronanostructure Integrating SiC Nanowires with MoS2 Nanosheets for Efficient Electrocatalytic Hydrogen Evolution. *ACS Appl. Mater. Interfaces* **2020**, *12* (17), 19519−19529.

(31) Zhou, X.; Li, X.; Gao, Q.; Yuan, J.; Wen, J.; Fang, Y.; Liu, W.; Zhang, S.; Liu, Y. Metal-Free Carbon Nanotube-SiC Nanowire Heterostructures with Enhanced Photocatalytic H2 Evolution under Visible Light Irradiation. *Catal. Sci. Technol.* **2015**, *5* (5), 2798−2806.

(32) Guo, X.; Tong, X.; Wang, Y.; Chen, C.; Jin, G.; Guo, X.-Y. High Photoelectrocatalytic Performance of a MoS2-SiC Hybrid Structure for Hydrogen Evolution Reaction. *J. Mater. Chem. A* **2013**, *1* (15), 4657−4661.

(33) Nariki, Y.; Inoue, Y.; Tanaka, K. Production of Ultra Fine SiC Powder from SiC Bulk by Arc-Plasma Irradiation under Different Atmospheres and Its Application to Photocatalysts. *J. Mater. Sci.* **1990**, *25* (7), 3101−3104.

(34) Jiang, M.; Liao, X.; Ding, L.; Chen, J. The Flexible SiC Nanowire Paper Electrode as Highly Efficient Photocathodes for Photoelectrocatalytic Water Splitting. *J. Electroanal. Chem.* **2017**, *806*, 61−67.

(35) Han, X.; Heuser, S.; Tong, X.; Yang, N.; Guo, X.-Y.; Jiang, X. Epitaxial Cubic Silicon Carbide Photocathodes for Visible-Light-Driven Water Splitting. *Chem. - Eur. J.* **2020**, *26* (16), 3586−3590.

(36) Liu, H.; She, G.; Mu, L.; Shi, W. Porous SiC Nanowire Arrays as Stable Photocatalyst for Water Splitting under UV Irradiation. *Mater. Res. Bull.* **2012**, *47* (3), 917−920.

(37) Shen, X.; Pantelides, S. T. Atomic-Scale Mechanism of Efficient Hydrogen Evolution at SiC Nanocrystal Electrodes. *J. Phys. Chem. Lett.* **2013**, *4* (1), 100−104.

(38) Lessio, M.; Carter, E. A. What Is the Role of Pyridinium in Pyridine-Catalyzed CO2 Reduction on p-GaP Photocathodes? *J. Am. Chem. Soc.* **2015**, *137* (41), 13248−13251.

(39) Du, J.; Wen, B.; Melnik, R. Mechanism of Hydrogen Production via Water Splitting on 3C-SiC's Different Surfaces: A First-Principles Study. *Comput. Mater. Sci.* **2014**, *95*, 451−455.

(40) Perdew, J. P.; Burke, K.; Ernzerhof, M. Generalized Gradient Approximation Made Simple. *Phys. Rev. Lett.* **1996**, *77* (18), 3865−3868.

(41) Sun, J.; Ruzsinszky, A.; Perdew, J. P. Strongly Constrained and Appropriately Normed Semilocal Density Functional. *Phys. Rev. Lett.* **2015**, *115* (3), 036402.

(42) Krukau, A. V.; Vydrov, O. A.; Izmaylov, A. F.; Scuseria, G. E. Influence of the Exchange Screening Parameter on the Performance of Screened Hybrid Functionals. *J. Chem. Phys.* **2006**, *125* (22), 224106.

(43) Kresse, G.; Joubert, D. From Ultrasoft Pseudopotentials to the Projector Augmented-Wave Method. *Phys. Rev. B: Condens. Matter Mater. Phys.* **1999**, *59* (3), 1758−1775.

(44) Monkhorst, H. J.; Pack, J. D. Special Points for Brillouin-Zone Integrations. *Phys. Rev. B* **1976**, *13* (12), 5188−5192.

(45) Henkelman, G.; Uberuaga, B. P.; Jónsson, H. A Climbing Image Nudged Elastic Band Method for Finding Saddle Points and Minimum Energy Paths. *J. Chem. Phys.* **2000**, *113* (22), 9901−9904.

(46) Sheppard, D.; Xiao, P.; Chemelewski, W.; Johnson, D. D.; Henkelman, G. A Generalized Solid-State Nudged Elastic Band Method. *J. Chem. Phys.* **2012**, *136* (7), 074103.

(47) Henkelman, G.; Jónsson, H. A Dimer Method for Finding Saddle Points on High Dimensional Potential Surfaces Using Only First Derivatives. *J. Chem. Phys.* **1999**, *111* (15), 7010−7022.

(48) Peng, S.; Jiang, Y.; Xu, C.; Hu, S.; Wang, Y. Surface Stabilities of 3C-SiC and H2O Adsorption on the (110)Surface. *J. Am. Ceram. Soc.* **2019**, *102* (10), 6256−6266.

(49) Toroker, M. C.; Kanan, D. K.; Alidoust, N.; Isseroff, L. Y.; Liao, P.; Carter, E. A. First Principles Scheme to Evaluate Band Edge Positions in Potential Transition Metal Oxide Photocatalysts and Photoelectrodes. *Phys. Chem. Chem. Phys.* **2011**, *13* (37), 16644−16654.

(50) Fuchs, F.; Furthmüller, J.; Bechstedt, F.; Shishkin, M.; Kresse, G. Quasiparticle Band Structure Based on a Generalized Kohn-Sham Scheme. *Phys. Rev. B: Condens. Matter Mater. Phys.* **2007**, *76* (11), 115109.

(51) Shishkin, M.; Kresse, G. Self-Consistent GW Calculations for Semiconductors and Insulators. *Phys. Rev. B: Condens. Matter Mater. Phys.* **2007**, *75* (23), 235102.

(52) Trasatti, S. The Absolute Electrode Potential: An Explanatory Note (Recommendations 1986). *Pure Appl. Chem.* **1986**, *58* (7), 955−966.

(53) Hörmann, N. G.; Andreussi, O.; Marzari, N. Grand Canonical Simulations of Electrochemical Interfaces in Implicit Solvation Models. *J. Chem. Phys.* **2019**, *150* (4), 041730.

(54) Nozik, A. J.; Memming, R. Physical Chemistry of Semiconductor-Liquid Interfaces. *J. Phys. Chem.* **1996**, *100* (31), 13061−13078.

(55) Nørskov, J. K.; Rossmeisl, J.; Logadottir, A.; Lindqvist, L.; Kitchin, J. R.; Bligaard, T.; Jónsson, H. Origin of the Overpotential for Oxygen Reduction at a Fuel-Cell Cathode. *J. Phys. Chem. B* **2004**, *108* (46), 17886−17892.

(56) Sundararaman, R.; Letchworth-Weaver, K.; Schwarz, K. A.; Gunceler, D.; Ozhabes, Y.; Arias, T. A. JDFTx: Software for Joint Density-Functional Theory. *SoftwareX* **2017**, *6*, 278−284.

(57) Van den Bossche, M.; Skúlason, E.; Rose-Petruck, C.; Jónsson, H. Addition to "Assessment of Constant-Potential Implicit Solvation Calculations of Electrochemical Energy Barriers for H2 Evolution on Pt. *J. Phys. Chem. C* **2019**, *123* (25), 15875−15875.

(58) Grahame, D. C. The Electrical Double Layer and the Theory of Electrocapillarity. *Chem. Rev.* **1947**, *41* (3), 441−501.

(59) Resasco, J.; Chen, L. D.; Clark, E.; Tsai, C.; Hahn, C.; Jaramillo, T. F.; Chan, K.; Bell, A. T. Promoter Effects of Alkali Metal Cations on the Electrochemical Reduction of Carbon Dioxide. *J. Am. Chem. Soc.* **2017**, *139* (32), 11277−11287.

(60) Sundararaman, R.; Goddard, W. A. The Charge-Asymmetric Nonlocally Determined Local-Electric (CANDLE) Solvation Model. *J. Chem. Phys.* **2015**, *142* (6), 064107.

(61) Nishihara, S.; Otani, M. Hybrid Solvation Models for Bulk, Interface, and Membrane: Reference Interaction Site Methods Coupled with Density Functional Theory. *Phys. Rev. B: Condens. Matter Mater. Phys.* **2017**, *96* (11), 115429.

(62) Lauermann, I.; Memming, R.; Meissner, D. Electrochemical Properties of Silicon Carbide. *J. Electrochem. Soc.* **1997**, *144* (1), 73.

(63) Skúlason, E. Modeling Electrochemical Reactions at the Solid-Liquid Interface Using Density Functional Calculations. *Procedia Comput. Sci.* **2015**, *51*, 1887−1896.

(64) Zhuang, H.; Yang, N.; Zhang, L.; Fuchs, R.; Jiang, X. Electrochemical Properties and Applications of Nanocrystalline, Microcrystalline, and Epitaxial Cubic Silicon Carbide Films. *ACS Appl. Mater. Interfaces* **2015**, *7* (20), 10886−10895.

(65) Rappoport, D.; Crawford, N. R. M.; Furche, F.; Burke, K. Approximate Density Functionals: Which Should I Choose? In *Computational Inorganic and Bioinorganic Chemistry*; Solomon, E., Scott, R., King, R. B., Eds.; Wiley: New York, 2011; pp 159−172.

(66) Sun, J.; Remsing, R. C.; Zhang, Y.; Sun, Z.; Ruzsinszky, A.; Peng, H.; Yang, Z.; Paul, A.; Waghmare, U.; Wu, X.; et al. Accurate First-Principles Structures and Energies of Diversely Bonded Systems from an Efficient Density Functional. *Nat. Chem.* **2016**, *8* (9), 831−836.

(67) Bronsted, J. N. Acid and Basic Catalysis. *Chem. Rev.* **1928**, *5* (3), 231−338.

(68) Evans, M. G.; Polanyi, M. Inertia and Driving Force of Chemical Reactions. *Trans. Faraday Soc.* **1938**, *34* (0), 11−24.

(69) Skúlason, E.; Tripkovic, V.; Björketun, M. E.; Gudmundsdóttir, S.; Karlberg, G.; Rossmeisl, J.; Bligaard, T.; Jónsson, H.; Nørskov, J. K. Modeling the Electrochemical Hydrogen Oxidation and Evolution Reactions on the Basis of Density Functional Theory Calculations. *J. Phys. Chem. C* **2010**, *114* (42), 18182−18197.

(70) Hao, J.-Y.; Wang, Y.-Y.; Tong, X.-L.; Jin, G.-Q.; Guo, X.-Y. Photocatalytic Hydrogen Production over Modified SiC Nanowires under Visible Light Irradiation. *Int. J. Hydrogen Energy* **2012**, *37* (20), 15038−15044.

(71) Nie, X.; Esopi, M. R.; Janik, M. J.; Asthagiri, A. Selectivity of CO2 Reduction on Copper Electrodes: The Role of the Kinetics of Elementary Steps. *Angew. Chem.* **2013**, *125* (9), 2519−2522.

(72) Häller, L. J. L.; Page, M. J.; Macgregor, S. A.; Mahon, M. F.; Whittlesey, M. K. Activation of an Alkyl C-H Bond Geminal to an Agostic Interaction: An Unusual Mode of Base-Induced C-H Activation. *J. Am. Chem. Soc.* **2009**, *131* (13), 4604−4605.

(73) Xu, S.; Carter, E. A. Balancing Competing Reactions in Hydride Transfer Catalysis via Catalyst Surface Doping: The Ionization Energy Descriptor. *J. Am. Chem. Soc.* **2019**, *141* (25), 9895−9901.

(74) Xu, S.; Carter, E. A. Optimal Functionalization of a Molecular Electrocatalyst for Hydride Transfer. *Proc. Natl. Acad. Sci. U. S. A.* **2019**, *116* (46), 22953−22958.